GEOLOGY | THE GEOLOGICAL SOCIETY OF AMERICA®

https://doi.org/10.1130/G49388.1

Manuscript received 4 December 2020
Revised manuscript received 1 August 2021
Manuscript accepted 10 August 2021

Published online 8 October 2021

Lateral variation in slab window viscosity inferred from global navigation satellite system (GNSS)–observed uplift due to recent mass loss at Patagonia ice fields

Raymond M. Russo[1], Haipeng Luo[2], Kelin Wang[2,3], Boudewijn Ambrosius[4], Victor Mocanu[5]*, Jiangheng He[3], Thomas James[2,3], Michael Bevis[6] and Rui Fernandes[7]

[1]Department of Geological Sciences, University of Florida, Gainesville, Florida 32608, USA
[2]School of Earth and Ocean Sciences, University of Victoria, Victoria, British Columbia V8W 2Y2, Canada
[3]Pacific Geoscience Centre, Geological Survey of Canada, Sidney, British Columbia V8L 4B2, Canada
[4]Faculty of Aerospace Engineering, Delft University of Technology, Kluyverweg 1, 2629 HS, Delft, Netherlands
[5]Department of Geophysics, University of Bucharest, RO-020956, Bucharest, Romania
[6]School of Earth Sciences, Ohio State University, Columbus, Ohio 43210, USA
[7]Instituto D. Luiz, University of Beira Interior, Rua Marquês d'Ávila e Bolama, 6201-001 Covilhã, Portugal

ABSTRACT

The geographic coincidence of the Chile Ridge slab window and the Patagonia ice fields offers a unique opportunity for assessing the effects of slab window rheology on glacial isostatic adjustment (GIA). Mass loss of these ice fields since the Little Ice Age causes rapid but variable crustal uplift, 12–24 mm/yr around the North Patagonia ice field, increasing to a maximum of 41 mm/yr around the South Patagonia ice field, as determined from newly collected or processed geodetic data. We used these observational constraints in a three-dimensional Maxwell viscoelastic finite element model of GIA response above both the subducting slab and slab window in which the upper-mantle viscosity was parameterized to be uniform with depth. We found that the viscosity of the northern part of the slab window, ~2 × 10^{18} Pa·s, is lower than that of the southern part by approximately an order of magnitude. We propose that this along-strike viscosity contrast is due to late Cenozoic ridge subduction beneath the northern part of the slab window, which increases asthenospheric temperature and reduces viscosity.

INTRODUCTION

The Patagonian slab window, which developed as a consequence of the subduction of the Chile Ridge at the Chile triple junction (CTJ; ~46.5°S; Fig. 1A; Cande and Leslie, 1986; Breitsprecher and Thorkelson, 2009; Russo et al., 2010a, 2020b), lies beneath both the Northern and Southern Patagonia ice fields (NPI and SPI, respectively). However, the locus of Chile Ridge subduction has generally migrated northward since the Miocene to reach its current position (Fig. 1A), as various segments of the spreading ridge entered the Chile Trench. We hypothesize that the asthenosphere in the more recently formed northern slab window is warmer and less viscous than that in the southern window. Testing this hypothesis is the goal of this investigation.

Published seismic imaging of the slab window, confined to north of ~49°S, resolves P-wave velocities at depths from 50 to 250 km that are ~6% slower than those observed farther north (Fig. 1A; Russo et al., 2010b), implying low viscosities. Preliminary results from an ongoing seismic imaging project that samples a broader region suggest higher seismic velocities south of ~49°S (Mark et al., 2020), although the results await confirmation by more complete analyses. Recent mass loss from the ice fields developed above the slab window has led to glacial isostatic adjustment (GIA), and consequent rapid uplift rates are strong functions of upper-mantle viscosity. Using a combination of new and existing global navigation satellite system (GNSS) observations of uplift as constraints for GIA models, we were able to examine the north-south viscosity contrast within the slab window.

ICE MASS LOSS AND ITS GEODETIC SIGNATURE

Patagonia ice mass loss histories from a number of studies (e.g., Rignot et al., 2003; Chen et al., 2007; Ivins et al., 2011; Willis et al., 2012a, 2012b; Fig. S1A in the Supplemental Material[1]) were synthesized by Lange et al. (2014) into a representative ice-loss history (history B), which was translated into a history of uniform ice-thinning rate shown in Figure 2A. Lange et al. (2014) also constructed an alternative scenario (history A), in which most of the ice loss occurred prior to the 1940s. We used history B as the primary loading history in our modeling, but we also tested the effects of history A. According to a number of studies, the ice-thinning rates at the NPI and SPI, on average, were similar over the past few decades (Fig. S1B). For simplicity, we assumed the same thinning history for both ice fields for most of our modeling, but we also conducted additional tests to address uncertainties associated with this assumption.

GNSS data around the shrinking SPI reveal the fastest (>40 mm/yr) geodetically observed GIA uplift anywhere on Earth, consistent with rebound above an upper mantle with viscosity values of ~10^{18}–10^{19} Pa·s (Ivins and James,

*E-mail: vi_mo@yahoo.com

[1]Supplemental Material. Modeling method, Table S1 (newly obtained uplift rates for the ten continuous GNSS sites shown in Figure 1B), Table S2 (slab window viscosity values and RMS data), supplemental figures, and the weekly solutions for GNSS data used in the study. Please visit https://doi.org/10.1130/GEOL.S.16624558 to access the supplemental material, and contact editing@geosociety.org with any questions.

CITATION: Russo, R.M., et al., 2021, Lateral variation in slab window viscosity inferred from global navigation satellite system (GNSS)–observed uplift due to recent mass loss at Patagonia ice fields: Geology, v. 50, p. 111–115, https://doi.org/10.1130/G49388.1

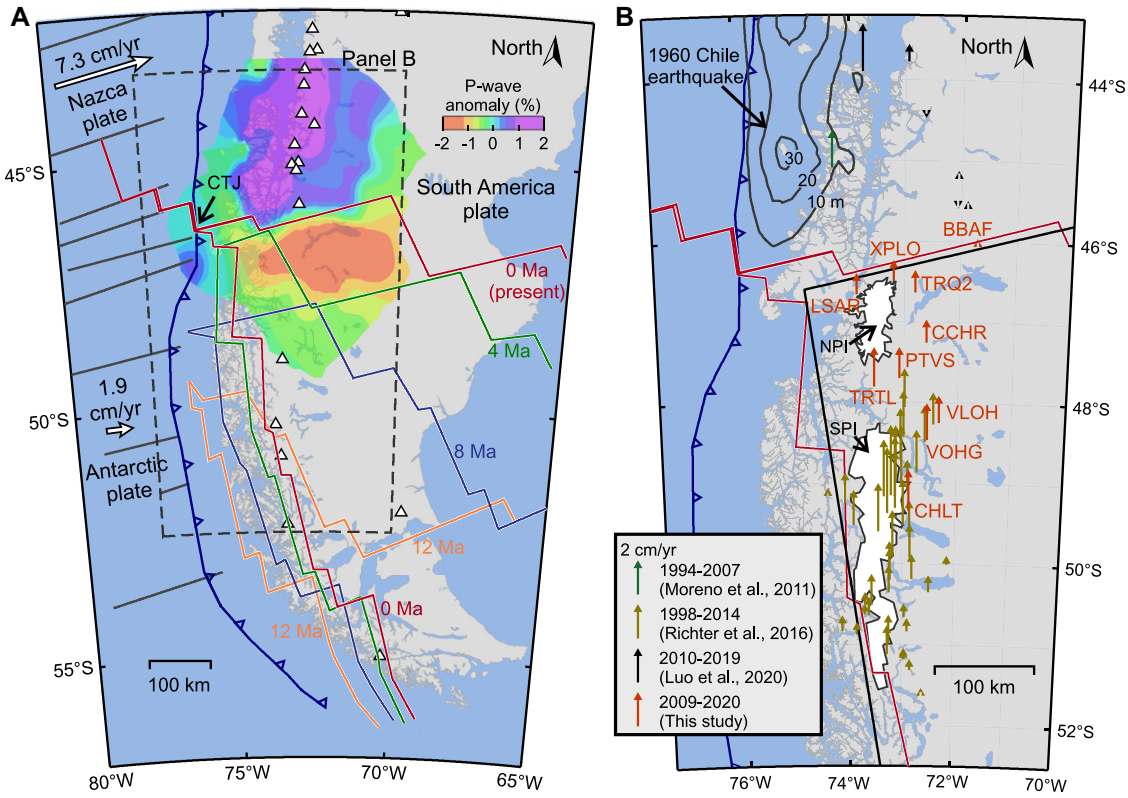

Figure 1. (A) Regional tectonic setting and slab window history of Patagonia, based on Breitsprecher and Thorkelson (2009). P-wave velocity anomalies at 100 km depth (Russo et al., 2010b) show contrast across the northern edge of the present slab window. Current plate motion vectors relative to the South America plate are from DeMets et al. (2010). Triangles are Holocene volcanos. CTJ—Chile triple junction. (B) Global navigation satellite system (GNSS) uplift rates. Red arrows labeled with station names show values determined in this work (Table S1 [see footnote 1]). Coseismic slip of the 1960 M 9.5 earthquake (gray contours) is from Ho et al. (2019). NPI, SPI—Northern and Southern Patagonia ice fields, respectively.

1999, 2004; Lange et al., 2014; Richter et al., 2016). However, these results are only valid for the SPI, situated above the early-formed part of the slab window (Fig. 1B), and they derive from modeling that was either one-dimensional (1-D; laterally homogeneous), neglecting the subduction zone structure (Ivins and James, 2004; Lange et al., 2014), or two-dimensional along an east-west profile crossing the SPI (Klemann et al., 2007) and thus not designed to resolve along-strike rheological variability. To test the hypothesis of variable viscosities in the slab window, we installed new GNSS stations around the previously undersampled NPI and processed other relevant GNSS data (Fig. 1B) to model the GIA response to the post–Little Ice Age mass loss histories of the entire Patagonian ice-field region.

New continuous GNSS observations at five sites installed by us in 2013 around the NPI (Fig. 1B), and post-2012 data from existing

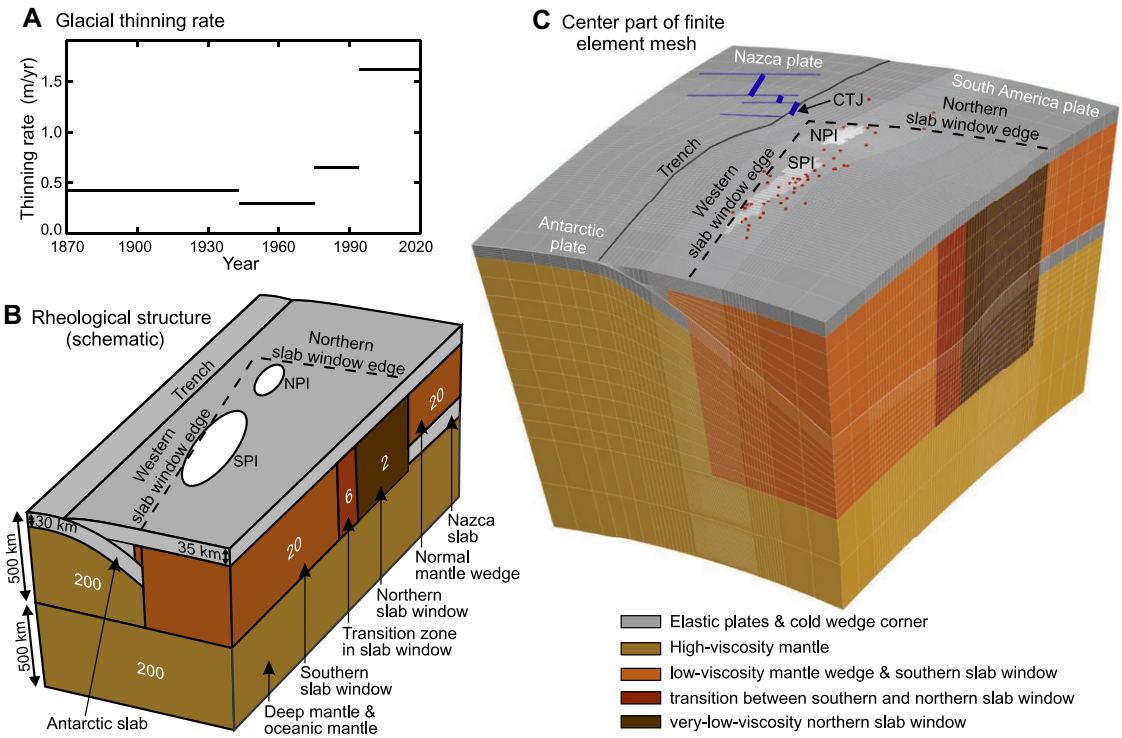

Figure 2. (A) Ice-thinning rate for both the Northern and Southern Patagonia ice fields (NPI/SPI) based on history B of Lange et al. (2014) (with small extrapolation to 2020). See Figure S1 (see footnote 1) for other proposed histories. (B) Model structure and rheology (not to scale). Viscosity (white numbers, in 10^{18} Pa·s) and thickness values are for the preferred model (Table S2). (C) Center part of finite element mesh. Each element has 27 nodes. Edges of slab have been simplified to straight lines (dashed). See Figure 1B for global navigation satellite system (GNSS) sites (red dots). CTJ—Chile triple junction.

GNSS stations (Blewitt et al., 2018) were processed using the GipsyX software (Bertiger et al., 2020). We used the International Terrestrial Reference Frame 2014 (ITRF14, https://www.iers.org/IERS/EN/DataProducts/ITRF/itrf.html) and computed velocities (red arrows in Fig. 1B; Table S1; Fig. S2) by fitting a linear trend plus seasonal terms. We also used campaign GNSS data from around the SPI (Richter et al., 2016) in our modeling. Potential differences in vertical rates (0–2 mm/yr) caused by the use of different reference frames in processing of these GNSS data sets was at least an order of magnitude less than observed uplift rates in the region (Fig. 1B).

MODELING GIA ABOVE THE SLAB WINDOW

Along-Strike Viscosity Contrast

We constructed finite element models with Maxwell viscoelasticity (see the Supplemental Material) to assess the GIA-induced uplift in the presence of the Patagonia slab window (Figs. 2B and 2C). Previous modeling (Wang et al., 2007; Moreno et al., 2011; Luo et al., 2020) suggested that vertical deformation due to megathrust earthquake cycles is negligibly small at the NPI and SPI relative to GIA deformation. To test the hypothesis stated in the Introduction, we allowed two areas of uniform viscosity within the slab window with a 1°-wide zone of transition in between (Figs. 2B and 2C). With trial-and-error, we found the optimal location of the center line of the transition zone to be 49°S. Recent independent seismic imaging (Mark et al., 2020) supports this choice.

Our preferred model best fits the GNSS observations (Figs. 3A and 3B; Table S2). A comparison with the 1-D model of Lange et al. (2014), incorporating model-predicted horizontal motion as well, is shown in Figure S3. Errors in the GNSS data around SPI are large because they are campaign measurements (Richter et al., 2016), but the many campaign sites collectively provide good model constraints (Fig. 3B). The preferred model features a factor of 10 contrast in upper-mantle viscosity between the northern (2×10^{18} Pa·s) and southern (2×10^{19} Pa·s) parts of the slab window; the higher viscosity of the southern window is equivalent to "normal" mantle wedge outside the window (Fig. 2B) and is comparable to other active tectonic regions (e.g., James et al., 2009; Austermann et al., 2020). However, the viscosity beneath the NPI is decidedly low, comparable only to upper-mantle viscosity in regions where Cenozoic ridge subduction has taken place (e.g., Larsen et al., 2005; Nield et al., 2014) or on Iceland, where a plume–spreading ridge interaction is ongoing (Pagli et al., 2007).

Models without an along-strike viscosity contrast in the slab window cannot simultaneously explain GNSS observations around both the NPI and SPI, as shown in Figure 3C. The required along-strike viscosity contrast is insensitive to structural details of the model. The upper-plate thickness of 35 km in the preferred model is consistent with the seismic imaging study of Rodriguez and Russo (2020) and earlier GIA models (Ivins et al., 2011; Lange et al., 2014; Richter et al., 2016). Uniformly changing the upper-plate thickness by 10 km would necessitate changing the slab-window viscosities by a factor of ~1.3 but would not eliminate the large along-strike contrast. A model with upper-plate thickness of 25 km in the north but 45 km in the south still requires a viscosity contrast of ~6.4 times to fit the GNSS data (Fig. S4A). If we

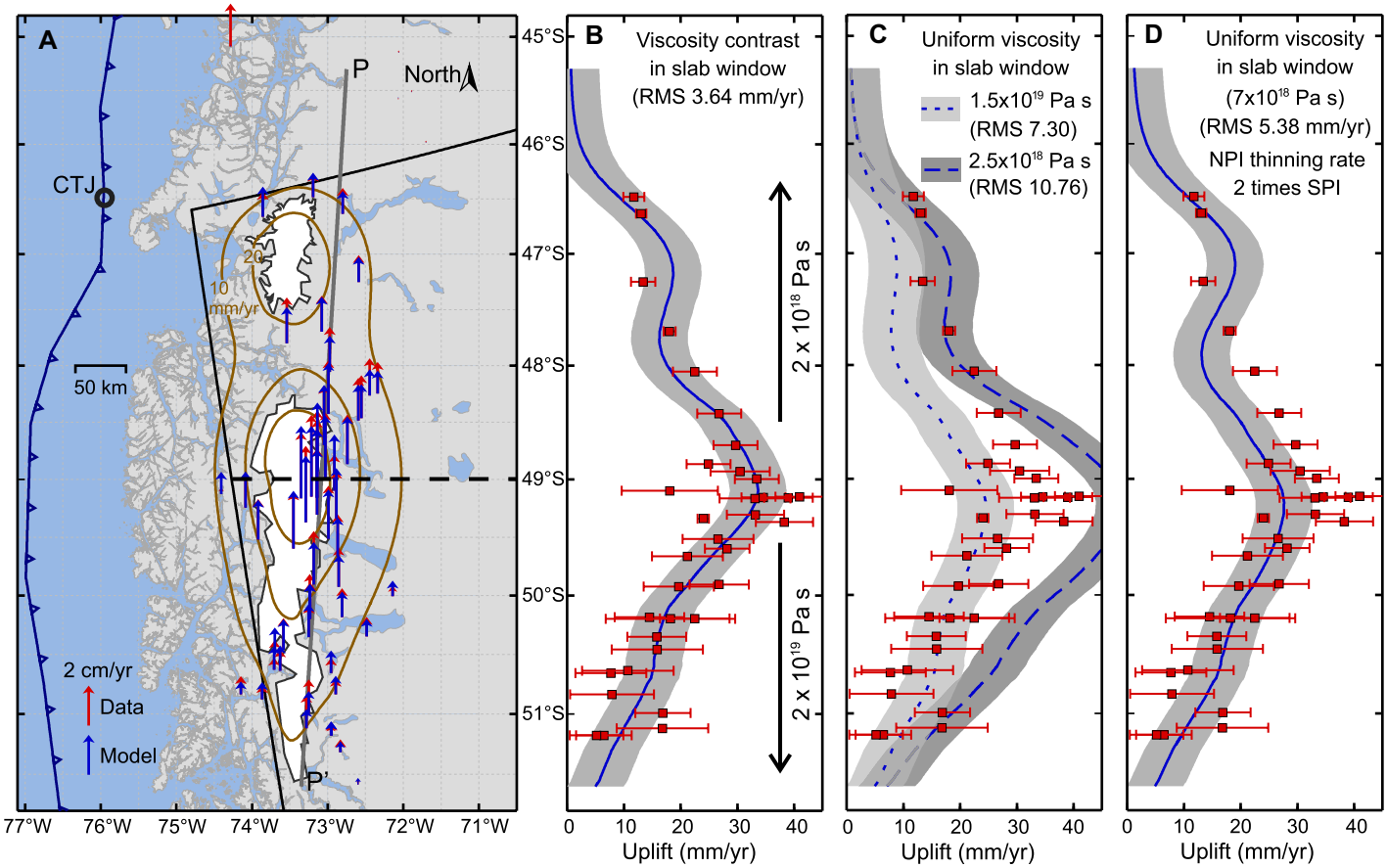

Figure 3. (A) Uplift rates (brown contours) predicted by our preferred model (Fig. 2B) and global navigation satellite system (GNSS) observations. Dashed line marks the center of 1°-wide viscosity transition (Table S2 [see footnote 1]). (B) Model uplift rates in A along profile P-P′ (blue curve) ± 5 mm/yr (gray area). GNSS values with 1σ error bars are from within 30 km of profile. Viscosity values show north-south contrast. (C) Model uplift rates but for models of uniform viscosity in the slab window. (D) Model of uniform viscosity but with contrasting ice-thinning rates (Fig. S1D). RMS—root-mean-square fit of model results to data (in mm/yr); NPI/SPI—Northern/Southern Patagonia ice fields.

neglect the subduction zone and use a layered-Earth model, including lateral variations, a large along-strike contrast in upper-mantle viscosity is still required to fit the data (Fig. S4B). The root-mean-square (RMS) values of the differences between model and GNSS uplift rates for the subduction zone models are shown in Table S2 and various figures.

Uncertainties in Ice-Loss History

Uncertainties in the ice mass loss history affect the estimated degree of the along-strike viscosity contrast, but they do not negate the requirement of the contrast. If we employ alternative ice-loss history A of Lange et al. (2014) (Fig. S1C), the required viscosity contrast is even greater than in the preferred model (Fig. S4C). Because the mass loss during recent decades in history A is slower than that in history B by a factor of ~2.5, viscosities required to fit the GNSS uplift rates are much lower, 10^{17} Pa·s and 3×10^{18} Pa·s for the northern and southern windows, respectively (Table S2).

Although available observations are more consistent with both ice fields thinning at similar rates for most of the past few decades, there is indication that the NPI rate may have exceeded the SPI rate since ca. 2010 (Fig. S1B). The effect of this recent change may be the largest source of uncertainty in our results, since our sensitivity tests (not displayed) indicate that post-2010 ice loss accounts for ~50% of the model-predicted uplift rates in Figure 3A. However, the present large scatter of estimated thinning rates (Fig. S1B) does not allow a more quantitative assessment of this effect. Instead, we constructed a model with NPI ice-thinning rate that is always twice the SPI rate (Fig. S1C). The combined mass loss rate equals that of the preferred model (history B). With a uniform slab-window viscosity of 7×10^{18} Pa·s, this model can marginally fit the overall GNSS pattern (Fig. 3D), but it systematically underestimates the uplift rates immediately north of 49°S, suggesting the need for a lower viscosity in this area.

DISCUSSION

Geodetic data north and south of the CTJ clearly show the dominance of two different tectonic processes. North of the CTJ (Fig. 4), the plate margin is primarily affected by rapid subduction of the Nazca plate, and geodetic measurements there generally reflect both megathrust earthquake cycles and permanent deformation of South America due to convergence. Postseismic deformation due to the 1960 Mw = 9.5 megathrust earthquake is the prevalent geodetic signal observed (Plafker and Savage, 1970; Wang et al., 2007; Moreno et al., 2011; Luo et al., 2020). South of the CTJ, slow subduction and limited Antarctic slab extent minimize the effects of plate convergence. Instead, available geodetic data predominantly reflect rapid GIA above the slab window. A contrast in mantle viscosity north and south of the CTJ has been suggested by previous seismic imaging (Fig. 1A). Our new results show that a viscosity contrast is present also within the slab window.

Although our model is the first GIA model to include three-dimensional subduction zone structure, it maintains the simplicity of the earlier 1-D model of Lange et al. (2014) in terms of mantle viscosity parameterization. The Lange et al. (2014) model (Fig. S3B) features an elastic plate overlying a uniform viscoelastic half space, and their preferred viscosity based on ice-loss history B is 8×10^{18} Pa·s. Richter et al. (2016) found that this model systematically underpredicted uplift rates in the northernmost SPI and overpredicted uplift rates for the rest of the SPI. We can readily verify this misfit pattern if we also assume a uniform viscosity of 8×10^{18} Pa·s, which is between the two uniform values in Figure 3C, for the slab window. This strongly supports the need to invoke nonuniform viscosity within the slab window (Fig. 3B).

Subduction of the actively spreading Chile Ridge advects hot upper mantle to shallow depths beneath South America. Models of thermal anomalies due to ridge subduction without active mantle flow—thus prescribing minimum temperature increases—show elevation of the geotherm by 150–250 °C in the mantle wedge between depths of 40 and 150 km, and the thermal effects can persist for up to 30 m.y. (Iwamori, 2000). Temperatures in the subducted slab increase similarly, and adakitic slab melts are possible. Predicted temperatures in the asthenospheric slab window are likely to be significantly higher if modeling includes mantle flow advecting heat into the slab window (DeLong et al., 1979). Thus, both advected hot mantle of the spreading ridge and asthenospheric upwelling to fill the slab window bring the slab window upper mantle closer to solidus and decrease its viscosity. This effect is the strongest north of 49°S in the youngest part of the slab window (Fig. 1A).

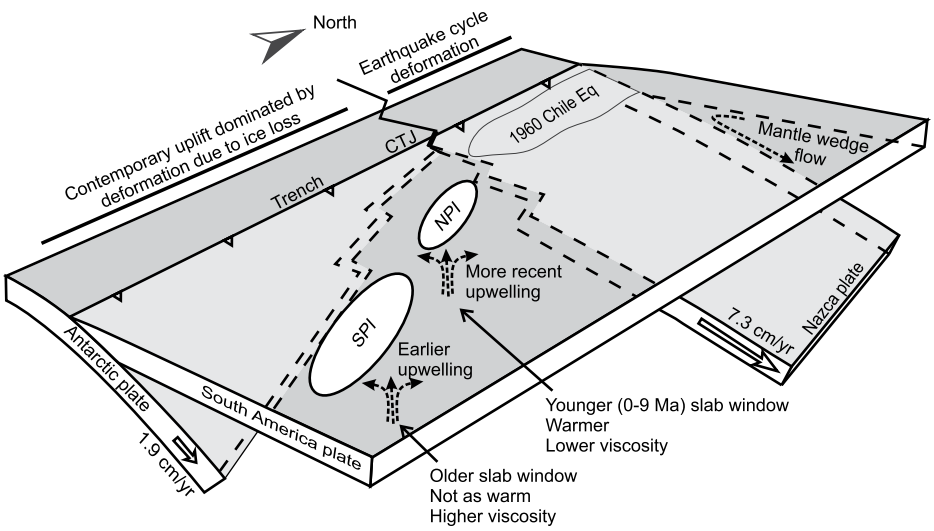

Figure 4. Geodynamics and crustal deformation in the region of the Chile triple junction (CTJ). North of the CTJ, deformation is dominated by megathrust earthquake (Eq) cycles. South of the CTJ, glacial isostatic adjustment (GIA) deformation at the Northern and Southern Patagonia ice fields (NPI and SPI, respectively) suggests viscosity contrast of one order of magnitude between these two parts of the slab window. More complex three-dimensional flow due to slab window migration and other tectonic processes is not shown.

CONCLUSION

New GNSS data from the NPI area, in combination with published data from the SPI, allowed us to test the hypothesis of an along-strike rheology contrast in the Patagonia slab window. Assuming ice-thinning rates are the same for both ice fields, GNSS-observed GIA uplift rates are consistent with an upper-mantle viscosity of 2×10^{18} Pa·s for the more recently developed, northern part of the slab window, and an order-of-magnitude higher value in the southern part. This large along-strike viscosity contrast is insensitive to details in assumed model structure. With a uniform viscosity, even an assumed NPI ice-thinning rate twice that of the SPI cannot satisfactorily explain the GNSS data. Details of the ice-thinning history of the most recent decade that are not addressed by our modeling may affect the degree, but not the presence, of the viscosity contrast. Our results support the notion that advected hot mantle due to ridge subduction and asthenospheric upwelling in the wake of the northward migration of the Nazca edge of the slab window caused a viscosity decrease in the slab window.

ACKNOWLEDGMENTS

We thank Sergio Barrientos, Juan Carlos Baez of Universidad de Chile, Gonzalo Hermosilla of

Servicio Nacional de Geología y Minería (Chile), Pablo Keupuchur, Ian Farmer, Don Gustavo, Cristina López Quintana, and Raul Tarnovschi for field support. Andrea Valenzuela, Adrián Escobar, Gabriela Gomez, and national park guards at Laguna San Rafael, Corporación Nacional Forestal (Chile), aided with permitting. Don Cirilo, Oscar Molinos, Artemio Perez, and Isidro Rivas gave permission to install global navigation satellite system stations. Hans van der Marel of Technische Universiteit Delft (TU Delft, Netherlands) and George Slad, Greg Chavez, and Noel Barstow of Incorporated Research Institutions for Seismology (IRIS) Portable Array Seismic Studies of the Continental Lithosphere (PASSCAL) helped with the station power setup. TU Delft provided equipment and partial funding for the field work. We thank Xin Zhou for collaboration in benchmarking our code, and five anonymous reviewers for comments.

REFERENCES CITED

Austermann, J., Chen, C.Y., Lau, H.C., Maloof, A.C., and Latychev, K., 2020, Constraints on mantle viscosity and Laurentide ice sheet evolution from pluvial paleolake shorelines in the western United States: Earth and Planetary Science Letters, v. 532, 116006, https://doi.org/10.1016/j.epsl.2019.116006.

Bertiger, W., et al., 2020, GipsyX/RTGx, a new tool set for space geodetic operations and research: Advances in Space Research, v. 66, p. 469–489, https://doi.org/10.1016/j.asr.2020.04.015.

Blewitt, G., Hammond, W.C., and Kreemer, C., 2018, Harnessing the GPS data explosion for interdisciplinary science: Eos, v. 99, p. 1–2, https://doi.org/10.1029/2018EO104623.

Breitsprecher, K., and Thorkelson, D.J., 2009, Neogene kinematic history of Nazca-Antarctic-Phoenix slab windows beneath Patagonia and the Antarctic Peninsula: Tectonophysics, v. 464, p. 10–20, https://doi.org/10.1016/j.tecto.2008.02.013.

Cande, S.C., and Leslie, R.B., 1986, Late Cenozoic tectonics of the southern Chile Trench: Journal of Geophysical Research, v. 91, p. 471–496, https://doi.org/10.1029/JB091iB01p00471.

Chen, J.L., Wilson, C.R., Tapley, B.D., Blankenship, D.D., and Ivins, E.R., 2007, Patagonia icefield melting observed by gravity recovery and climate experiment (GRACE): Geophysical Research Letters, v. 34, L22501, https://doi.org/10.1029/2007GL031871.

DeLong, S.E., Wschwarz, W.M., and Anderson, R.N., 1979, Thermal effects of ridge subduction: Earth and Planetary Science Letters, v. 44, p. 239–246, https://doi.org/10.1016/0012-821X(79)90172-9.

DeMets, C., Gordon, R.G., and Argus, D.F., 2010, Geologically current plate motion: Geophysical Journal International, v. 181, p. 1–80, https://doi.org/10.1111/j.1365-246X.2009.04491.x.

Ho, T.C., Satake, K., Watada, S., and Fujii, Y., 2019, Source estimate for the 1960 Chile earthquake from joint inversion of geodetic and transoceanic tsunami data: Journal of Geophysical Research: Solid Earth, v. 124, p. 2812–2828, https://doi.org/10.1029/2018JB016996.

Ivins, E.R., and James, T.S., 1999, Simple models for late Holocene and present-day Patagonian glacier fluctuations and predictions of a geodetically detectable isostatic response: Geophysical Journal International, v. 138, p. 601–624, https://doi.org/10.1046/j.1365-246x.1999.00899.x.

Ivins, E.R., and James, T.S., 2004, Bedrock response to Llanquihue Holocene and present-day glaciation in southernmost South America: Geophysical Research Letters, v. 31, L24613, https://doi.org/10.1029/2004GL021500.

Ivins, E.R., Watkins, M.M., Yuan, D.-N., Dietrich, R., Casassa, G., and Rülke, A., 2011, On-land ice loss and glacial isostatic adjustment at the Drake Passage: 2003–2009: Journal of Geophysical Research, v. 116, B02403, https://doi.org/10.1029/2010JB007607.

Iwamori, H., 2000, Thermal effects of ridge subduction and its implications for the origin of granitic batholith and paired metamorphic belts: Earth and Planetary Science Letters, v. 181, p. 131–144, https://doi.org/10.1016/S0012-821X(00)00182-5.

James, T.S., Gowan, E.J., Wada, I., and Wang, K., 2009, Viscosity of the asthenosphere from glacial isostatic adjustment and subduction dynamics at the northern Cascadia subduction zone, British Columbia, Canada: Journal of Geophysical Research: Solid Earth, v. 114, B04405, https://doi.org/10.1029/2008JB006077.

Klemann, V., Ivins, E.R., Martinec, Z., and Wolf, D., 2007, Models of active glacial isostasy roofing warm subduction: Case of the South Patagonian ice field: Journal of Geophysical Research: Solid Earth, v. 112, B09405, https://doi.org/10.1029/2006JB004818.

Lange, H., Casassa, G., Ivins, E.R., Schröder, L., Fritsche, M., Richter, A., Groh, A., and Dietrich, R., 2014, Observed crustal uplift near the Southern Patagonian icefield constrains improved viscoelastic Earth models: Geophysical Research Letters, v. 41, p. 805–812, https://doi.org/10.1002/2013GL058419.

Larsen, C.F., Motyka, R.J., Freymueller, J.T., Echelmeyer, K.A., and Ivins, E.R., 2005, Rapid viscoelastic uplift in southeast Alaska caused by post–Little Ice Age glacial retreat: Earth and Planetary Science Letters, v. 237, p. 548–560, https://doi.org/10.1016/j.epsl.2005.06.032.

Luo, H., Ambrosius, B., Russo, R.M., Mocanu, V., Wang, K., Bevis, M., and Fernandes, R., 2020, A recent increase in megathrust locking in the southernmost rupture area of the giant 1960 Chile earthquake: Earth and Planetary Science Letters, v. 537, 116200, https://doi.org/10.1016/j.epsl.2020.116200.

Mark, H.F., Wiens, D., Pourpoint, M., Magnani, M.B., Ivins, E.R., Richter, A., and Barrientos, S.E., 2020, Seismic structure and the extent of the slab window beneath the Northern and Southern Patagonia icefields: Washington, D.C., American Geophysical Union, Fall Meeting supplement, abstract G012–0016, https://agu.confex.com/agu/fm20/meetingapp.cgi/Paper/697721.

Moreno, M., et al., 2011, Heterogeneous plate locking in the south-central Chile subduction zone: Building up the next great earthquake: Earth and Planetary Science Letters, v. 305, p. 413–424, https://doi.org/10.1016/j.epsl.2011.03.025.

Nield, G.A., Barletta, V.R., Bordoni, A., King, M.A., Whitehouse, P.L., Clarke, P.J., Domack, E., Scambos, T.A., and Berthier, E., 2014, Rapid bedrock uplift in the Antarctic Peninsula explained by viscoelastic response to recent ice unloading: Earth and Planetary Science Letters, v. 397, p. 32–41, https://doi.org/10.1016/j.epsl.2014.04.019.

Pagli, C., Sigmundsson, F., Lund, B., Sturkell, E., Geirsson, H., Einarsson, P., Árnadóttir, T., and Hreinsdóttir, S., 2007, Glacio-isostatic deformation around the Vatnajökull ice cap, Iceland, induced by recent climate warming: GPS observations and finite element modeling: Journal of Geophysical Research: Solid Earth, v. 112, B08405, https://doi.org/10.1029/2006JB004421.

Plafker, G., and Savage, J.C., 1970, Mechanism of the Chilean earthquakes of May 21 and 22, 1960: Geological Society of America Bulletin, v. 81, p. 1001–1030, https://doi.org/10.1130/0016-7606(1970)81[1001:MOTCEO]2.0.CO;2.

Richter, A., et al., 2016, Crustal deformation across the Southern Patagonian icefield observed by GNSS: Earth and Planetary Science Letters, v. 452, p. 206–215, https://doi.org/10.1016/j.epsl.2016.07.042.

Rignot, E., Rivera, A., and Casassa, G., 2003, Contribution of the Patagonia icefields of South America to sea level rise: Science, v. 302, p. 434–437, https://doi.org/10.1126/science.1087393.

Rodriguez, E.E., and Russo, R.M., 2020, Southern Chile crustal structure from teleseismic receiver functions: Responses to ridge subduction and terrane assembly of Patagonia: Geosphere, v. 16, p. 378–391, https://doi.org/10.1130/GES01692.1.

Russo, R.M., Gallego, A., Comte, D., Mocanu, V.I., Murdie, R.E., and VanDecar, J.C., 2010a, Source-side shear wave splitting and upper mantle flow in the Chile Ridge subduction region: Geology, v. 38, p. 707–710, https://doi.org/10.1130/G30920.1.

Russo, R.M., VanDecar, J.C., Comte, D., Mocanu, V.I., Gallego, A., and Murdie, R.E., 2010b, Subduction of the Chile Ridge: Upper mantle structure and flow: GSA Today, v. 20, p. 4–10, https://doi.org/10.1130/GSATG61A.1.

Wang, K., Hu, Y., Bevis, M., Kendrick, E., Smalley, R.Jr., Vargas, R.B., and Lauría, E., 2007, Crustal motion in the zone of the 1960 Chile earthquake: Detangling earthquake-cycle deformation and forearc-sliver translation: Geochemistry Geophysics Geosystems, v. 8, Q10010, https://doi.org/10.1029/2007GC001721.

Willis, M.J., Melkonian, A.K., Pritchard, M.E., and Ramage, J.M., 2012a, Ice loss rates at the Northern Patagonian icefield derived using a decade of satellite remote sensing: Remote Sensing of Environment, v. 117, p. 184–198, https://doi.org/10.1016/j.rse.2011.09.017.

Willis, M.J., Melkonian, A.K., Pritchard, M.E., and Rivera, A., 2012b, Ice loss from the Southern Patagonian ice field, South America, between 2000 and 2012: Geophysical Research Letters, v. 39, L17501, https://doi.org/10.1029/2012GL053136.

Printed in USA